7
Publicação em Periódicos Internacionais

F. C. Fávero; Quintero, Sully M. M. ; Martelli, Cicero ; Braga, Arthur M.B. ; Silva, Vinícius V. ; Carvalho, Isabel C. S. ; Llerena, Roberth W. A. Valente, Luiz C. Guedes. "Hydrostatic Pressure Sensing with High Birefringence Photonic Crystal Fibers", $Sensors, 10, p. 9698 - 9711, 2010.$

F. C. Favero, Geraud Bouwmans, Vittoria Finazzi, Joel Villatoro, and Valerio Pruneri, "Photonic crystal fiber Fabry-Perot interferometer built by fusion splicing and voids pressurization" $Optics Letters$ 2011

F. C. Fávero, J. Villatoro, V. Pruneri, "Microstructured optical fiber interferometric breathing sensor" $Journal of Biomedical Optics$ 2012

F. C. Favero, L. F. Araujo, G. Bouwmans, V. Finazzi, J. Villatoro, and V. Pruneri, "Spheroidal Fabry-Perot microcavities in optical fibers for high-sensitivity sensing", $Optics Express$ 2012

Article

Hydrostatic Pressure Sensing with High Birefringence Photonic Crystal Fibers

Fernando C. Fávero [1], Sully M. M. Quintero [1], Cicero Martelli [1,2], Arthur M.B. Braga [1,*], Vinicius V. Silva [1], Isabel C. S. Carvalho [1], Roberth W. A. Llerena [1] and Luiz C. G. Valente [1]

[1] Pontifical Catholic University of Rio de Janeiro, Rua Marquês de São Vicente 225, 22453-900, Rio de Janeiro, RJ, Brazil; E-Mails: fc.favero@fis.puc-rio.br (F.C.F.); sully@aluno.puc-rio.br (S.M.M.Q); vinicius_v_silva@hotmail.com (V.V.S.); isabel.carvalho@puc-rio.br (I.C.S.C.); roberan@puc-rio.br (R.W.A.L); luizguedes@puc-rio.br (L.C.G.V.)

[2] Department of Electronics, Federal University of Technology-Parana, Av Monteiro Lobato, s/n–km 04-Ponta Grossa, PR, 84016-210, Brazil; E-Mail: cmartelli@utfpr.edu.br

* Author to whom correspondence should be addressed; E-Mail: abraga@puc-rio.br; Tel.: +55-21-35271181; Fax: +55-21-35271165.

Abstract: The effect of hydrostatic pressure on the waveguiding properties of high birefringence photonic crystal fibers (HiBi PCF) is evaluated both numerically and experimentally. A fiber design presenting form birefringence induced by two enlarged holes in the innermost ring defining the fiber core is investigated. Numerical results show that modal sensitivity to the applied pressure depends on the diameters of the holes, and can be tailored by independently varying the sizes of the large or small holes. Numerical and experimental results are compared showing excellent agreement. A hydrostatic pressure sensor is proposed and demonstrated using an in-fiber modal interferometer where the two orthogonally polarized modes of a HiBi PCF generate fringes over the optical spectrum of a broad band source. From the analysis of experimental results, it is concluded that, in principle, an operating limit of 92 MPa in pressure could be achieved with 0.0003% of full scale resolution.

1. Introduction

The sensitivity of high birefringence (HiBi) fibers to hydrostatic pressure has interested the scientific community as a feasible alternative for pressure sensing. The anisotropic nature of the core region, including stress distribution and geometry, makes HiBi fibers sensitive to axially symmetric transverse forces acting on the external surface of the fiber. HiBi photonic crystal fibers, where the degeneracy is lifted by a break in structural symmetry, present some important advantages over conventional stress induced HiBi optical fibers, and have recently been employed to demonstrate pressure sensors based on either intermodal interferometry [1-4] or Type II fiber Bragg gratings [5].

Conventional all-solid HiBi fibers present residual stresses that are largely dependent on material thermal relaxation, and consequently are highly sensitive to temperature variations. Temperature sensitivity in PCFs, on the other hand, is mostly associated to the fiber thermo-optic coefficient and can also be made negligible [6]. They can be specifically tailored to enhance their response to hydrostatic pressure while presenting negligible temperature dependence [7]. The internal microstructure of holey PCFs can be engineered to behave as an air-silica composite material, where size of holes and their distribution at the core and cladding regions of its cross section can increase or decrease response to strain, pressure, or temperature [8,9]. Another advantage concerning pure silica PCFs lies in their chemical resistance to hydrogen, which makes them particularly attractive for sensing applications in high temperature and hydrogen rich environments. The absence of defects induced by germanium or phosphorous doping in the glass matrix greatly enhances the fiber immunity to H_2 diffusion and reaction, which are both responsible for decreasing the fiber's transparency and mechanical strength [10].

The work presented here brings detailed information on the effect of hydrostatic pressure over the waveguiding properties of PCFs and also insight on ways of shaping the fiber sensitivity. Given the numerous design possibilities to achieve high birefringence with PCFs, a fiber design that is already available in the market was chosen as starting point and reference. Multiphysics finite element analysis is employed to numerically evaluate the coupled mechanical and optical response of HiBi PCFs to hydrostatic pressure. With the aid of a numerical model, we analyze in detail the changes in modal birefringence brought about by slight modifications in the design of the reference fiber. This same reference PCF is then employed to demonstrate a hydrostatic pressure sensor based on polarization mode interference within the fiber. Finally, numerical and experimental results are compared showing excellent agreement.

2. HiBi PCF Fiber Design and Numerical Modeling

There are distinct ways of tailoring PCFs to enhance their birefringence. This may be accomplished, for instance, by breaking the n-fold rotational symmetry of an otherwise n-fold symmetric holey microstructure [11]. In another approach, elliptical holes with equal or different sizes have been employed to define both the cladding and core regions of the PCF [12,13]. Birefringence as high as of the order of 10^{-2} can be achieved in this fashion. However, only a few of these fibers are commercially available at this time. Therefore, in this paper, we have resorted to a commercial HiBi PCF supplied by NKT Photonics. Their fiber model PM-1550-01 [14] was used here as a reference for numerical and experimental investigations. This same fiber has been employed elsewhere to demonstrate

pressure [1-4], strain [15], torsion [16], and magnetic sensors [17]. The cross-section of the fiber PM-1550-01, depicted in Figure 1(a), contains a hexagonal lattice of small holes defining the cladding region. A missing hole in the middle gives rise to a solid core. Due to the high index contrast between core and cladding regions, the guidance mechanism is predominantly governed by total internal reflection. The distance between holes forming the periodic lattice is $\Lambda = 4.4$ μm. The diameter of the small air holes is $d = 2.2$ μm. Birefringence is generated by replacing two of the small holes in the innermost ring surrounding the core by larger holes of nominal diameter $D = 4.5$ μm. The solid portion of the fiber is made of pure silica ($n_{SiO2} = 1.45$). In the numerical study reported here, we have analyzed geometrical variations of this reference PCF where d and D were either enlarged or reduced.

Figure 1. (a) Scanning electron microscopy picture of the pure silica HiBi PCF fiber used as reference for the numerical modeling and demonstration of a hydrostatic pressure sensor; (b) schematic representation of the fiber core showing the fast and slow axis as well as the stress components (σ_1 and σ_2); (c) mesh representing the fiber structure for the finite element analysis–inset: zoom in on the structured region defining the fiber core; (d) stress distribution (σ_2 component) across the fiber core; and (e) numerically calculated electric field distribution for one polarization eigenstate mode.
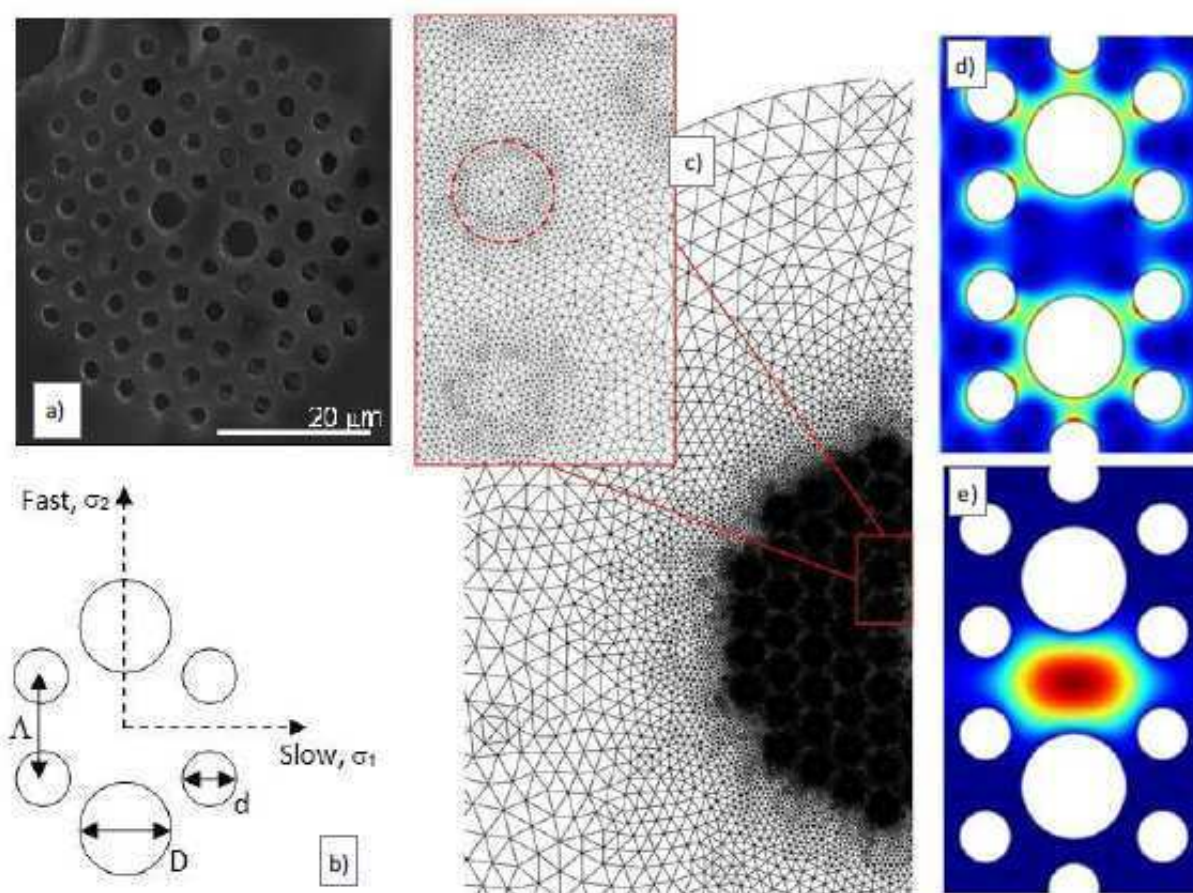
The stress distribution within the fiber and the propagation constants of the two confined modes under the action of hydrostatic pressure are calculated using the finite element code COMSOL Multiphysics® (version 3.5) [18]. As highlighted in Figure 1(b), the mesh density of the finite element model is higher near the structured region of the fiber cross-section. Satisfactory refinement was obtained after a convergence analysis lead to a mesh with 153,280 triangular elements. Figure 1(d,e) present examples of the stress and electric field distributions within the waveguide calculated using the finite element software.

The first step in order to assess the effect of hydrostatic pressure in the waveguiding properties of the PCF is a numerical evaluation of the stress distribution in the pressure loaded fiber. A state of plane-strain was assumed in the simulations, and the values employed for the silica glass' Young modulus and Poisson ratio were 72.5 GPa and 0.17 respectively. After obtaining the stress field due to the applied pressure, the new refractive index distribution in the fiber cross-section is evaluated by using the stress-optical relation [19]:

$$
\begin{aligned}
n_1 &= n_0 - C_1\sigma_1 - C_2(\sigma_2 + \sigma_3) \\
n_2 &= n_0 - C_1\sigma_2 - C_2(\sigma_1 + \sigma_3) \\
n_3 &= n_0 - C_1\sigma_3 - C_2(\sigma_1 + \sigma_2)
\end{aligned}
\tag{1}
$$

where σ_1, σ_2, and σ_3 are the principal stresses in the fiber, while C_1 and C_2 correspond to the stress-optical constants, which, for silica glass, are 0.69×10^{-12} and 4.2×10^{-12} Pa^{-1} in that order.

The new refractive index distribution, calculated for the pressure loaded fiber through Equation (1), is then used to numerically obtain the effective indices of the two orthogonally polarized fundamental modes ($LP_{01\text{-slow}}$ and $LP_{01\text{-fast}}$). The modal fields and effective indices are calculated using a full-vectorial model and the Maxwell's differential equation is expressed in terms of transverse electric and magnetic fields. In the numerical model, instead of resorting to a perfecly matching layer boundary condition, we have assumed a perfect magnetic conductor condition along the fiber's outermost boundary. This simpler condition could be employed here due to the fact that we are interested in simulating only the two fundamental LP_{01} modes, whose fields rapidly decay towards the computational boundary. Furthermore, these modes present negligible loss within the fiber lengths employed in the present investigation.

Phase and group modal birefringence, denoted as B and G respectively, are given by [6,7]:

$$
B = n_{LP01}^{slow} - n_{LP01}^{fast}
\tag{2}
$$

$$
G = B - \lambda\frac{dB}{d\lambda}
\tag{3}
$$

where n_{LP01}^{slow} and n_{LP01}^{fast} are the effective refractive indices of the two polarization modes and λ the wavelength.

2.1. Results and Discussion

The coupled elasto-optic response in the presence of hydrostatic pressure was numerically investigated for two groups of fibers. In the first group, the size of small holes forming the cladding was fixed at $d = 2.2$ μm, while the diameter of the two large holes, D, ranged from 4.2 to 5.1 μm. In the second group, the diameter of the two large holes was fixed at 4.5 μm while the sizes of small

Fabry–Perot interferometers built by photonic crystal fiber pressurization during fusion splicing

Fernando. C. Favero,[1,2] Geraud Bouwmans,[3] Vittoria Finazzi,[2] Joel Villatoro,[2,*] and Valerio Pruneri[3,4]

[1]*Pontifical Catholic University of Rio de Janeiro, Rua Marquês de São Vicente 225, 22453-900, Rio de Janeiro, RJ, Brazil*

[2]*ICFO—Institut de Ciencies Fotoniques, Mediterranean Technology Park, 08860, Castelldefels, Barcelona, Spain*

[3]*PhLAM/IRCICA—Laboratoire de Physique des Lasers Atomes et Molécules/Institut de Recherche sur les Composants logiciels et matériels pour l'Information et la Communication Avancée, Université Lille, CNRS UMR8523/USR3380, 59658 Villeneuve d'Ascq, France*

[4]*Also with ICREA-Institució Catalana de Recerca i Estudis Avançats, 08010, Barcelona, Spain*

*Corresponding author: joel.villatoro@icfo.es

We report on a microscopic Fabry–Perot interferometer whose cavity is a bubble trapped inside an optical fiber. The microcavity is formed by pressuring a photonic crystal fiber (PCF) with large voids during fusion splicing with a conventional single-mode fiber. The technique allows achieving high repeatability and full control over the cavity size and shape. It was found that the size of the PCF voids contributes to control the cavity size independently of the pressure in the PCF. Our devices exhibit a record fringe contrast of 30 dB (visibility of 0.999) due to the ellipsoidal cavity whose surfaces compensate for the diffraction of the reflected beam. The strain sensitivity of the interferometers is higher when the cavities are ellipsoidal than when they are spherical. © 2011 Optical Society of America

OCIS codes: 120.2230, 060.5295, 060.2370, 120.3180.

One of the simplest configurations of a Fabry–Perot interferometer (FPI) consists of two uncoated fiber ends separated by an air gap [1,2]. In such a configuration, the permanent alignment of the fibers imposes constraints, thus considerable research efforts have been placed on making the microcavity inside the fiber. For example, the cavity can be carved by means of chemical etching [3–5] or femtosecond laser micromachining [6,7]. Another alternative consists of splicing a short section of capillary tube or holey fiber between two single-mode fibers [8–11]. Some associated drawbacks of these approaches include costly equipment, multiple fabrication steps, reflecting surfaces with imperfections due to the removal of material, and/or low mechanical strength. By splicing a photonic crystal fiber (PCF) or a capillary tube and a conventional optical fiber using the standard arc-discharge technique, it is also possible to form a microscopic air cavity inside the waveguide [12–14]. The main disadvantage in this case is the low reproducibility and minimal control over the cavity length.

In this Letter we demonstrate high-quality microscopic FPIs. Their fabrication is carried out by pressurizing in a controlled manner a PCF during splicing with a standard optical fiber (SMF-28). The technique allows high reproducibility and control over the size and shape of the cavities. The micro-FPIs are entirely embedded in the fiber and exhibit record fringe contrast (30 dB) due to the ellipsoidal shape of the cavity. It was found that the size of the PCF voids also helps to control the cavity length of the interferometers. When the devices are used for strain sensing, substantial sensitivity improvements where found when the fabrication was via void pressurization.

Figure 1 shows the fabrication and characterization setup along with the cross section of two PCFs used in the experiments. The two PCFs had the same hole pattern and core/cladding diameter but different hole sizes. The average void diameter of PCF-A and PCF-B were, respectively, 4.8 and 5.6 μm. To fabricate the FPIs, the PCF and the standard fiber were spliced with a conventional fusion splicing machine (in our case with an Ericsson FSU 955). To have control over the cavity length, the voids of the PCF were pressurized with pure nitrogen using a homemade device.

It is known that, when an SMF and a PCF are fusion spliced, the PCF's air holes may entirely collapse [13]. As a result, part of the air (or nitrogen) originally inside the voids can be trapped, thus forming a microscopic cavity [12,13]. A collection of samples were fabricated at different pressures with a fusion program that had the following parameters: prefusion time, 0.3 s; prefusion arc, 13 mA; overlap, 5 μm; fusion current 1, 12 mA. The remaining parameters were those set in the machine for splicing SMFs. When the PCFs were not pressurized, the cavities had a spherical shape [12,13], but their sizes could not be controlled. However, when the PCF voids were pressurized, the cavities had an ellipsoidal shape (see Fig. 2) whose dimensions depended on the pressure. The short overlap and the pressure in the PCF contributed to achieve elliptical cavities. In all cases, the microbubbles were formed at the interface with the SMF, in
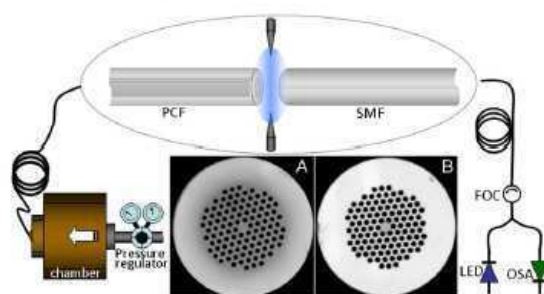

Fig. 1. (Color online) Drawing of the fabrication and characterization setup. LED stands for light emitting device, FOC for fiber optic circulator, and OSA for optical spectrum analyzer. The cross sections of the PCFs used are shown.

Fig. 2.   Micrographs of some cavities. (a) The PCF is not pressurized, (b) and (c) the pressure was 1.5 bars and 1.0 bar, respectively. d refers to cavity length. The fiber used was the PCF-B.

front of its core; see Fig. 2. The cavities were always formed when the PCF was pressurized.

In our devices, interference occurs between light reflected from a glass–air interface and that reflected from an air–glass interface. The reflectivity of each interface is ∼3.7%; hence, the transfer function of our FPI can be expressed as [15]: $I = I_1 + I_2 + 2\sqrt{I_1 I_2}\cos(\Delta\varphi)$, where I_1 and I_2 are, respectively, the intensity of the beam reflected from the SMF-end–air interface and the air–glass interface. $\Delta\varphi$ is the total phase, which, to a good approximation, can be expressed as $\Delta\varphi \approx 4\pi nd/\lambda$, n being the refractive index of the medium trapped inside the cavity and λ the wavelength of the optical source.

Figure 3 shows the reflection spectra of three devices. The difference in the fringe contrast when the cavities had elliptical shapes is evident. The fringe contrast or visibility of an interferometer is an important parameter, particularly when the interferometer is used for sensing or metrological applications. Typically, higher visibility is desirable since it leads to larger signal-to-noise ratio and more accurate measurement. The visibility (V) of a two-beam interferometer is calculated by [15]

$$V = 2\sqrt{k}/(1+k), \qquad (1)$$

where $k = I_2/I_1$. It can be noted that V can be as high as 1 if the two reflections have equal intensities. In fiber FPIs with flat reflecting surfaces, I_2 is always smaller than I_1 due to the loss introduced by the recoupling of the beam [16]. The recoupling loss is a consequence of the divergence of the propagating beam. The situation is similar in FPIs with small spherical cavities. However, as it is shown in Fig. 3, when the cavity has an ellipsoidal shape,

V enhances remarkably. The interfaces with large radius of curvature compensate partially the divergence of the reflected beam, thus V can be high. Note from Fig. 3 that the fringe contrast in our 28-μm-long cavity FPI reaches 30 dB ($V = 0.999$), which is, to our knowledge, the highest visibility reported until now for an FPI using reflections from silica–air interfaces. Around 75% of our FPIs with cavities in the 25–60 μm range exhibited visibilities in the 25–30 dB range.

Figure 4 shows the fringe spacing or period (P) of our devices along with the cavity size (measured under an optical microscope) as a function of pressure in the PCF voids. P was measured at 1550 nm and was calculated by the expression $P \approx \lambda^2/2nd$. Note that the period or cavity length of our FPIs can be controlled with the pressure since the medium inside the cavity does not change (air or nitrogen). Basically, by increasing the pressure when the PCF is heated, the voids are enlarged [17] and, thus, the cavity becomes bigger. Note that the PCF with larger voids (PCF-B) allows the fabrication of larger cavities. This suggests that the PCF void size contributes also to control P and/or d.

The temperature dependence of the interferometers was studied. The thermal sensitivity of the devices was found to be ∼1 pm/°C whatever the size of the cavity, which is consistent with the results reported in [13]. The application of the interferometers for strain sensing was also studied, placing emphasis on the dependence of the sensor sensitivities on d (or pressure in the PCF) and shape of the cavities. Figure 5 shows the shift of the interference patterns as a function of the applied strain observed in different interferometers. Because of the Poisson effect, the ellipsoid cavities of our FPIs undergo maximum elongation in the direction of stretching, which is also the direction of light propagation. The effect is more prominent as d becomes smaller and smaller, thus the strain sensitivity (slope of the curves) is higher in FPIs with short cavities. Because of the extremely low thermal sensitivity of our FPIs and their high strain sensitivity, the temperature-induced strain error is calculated to be of the order of 0.15 $\mu\varepsilon$/°C, thus fluctuations of ∼100 °C would be needed to induce an error of ∼15 $\mu\varepsilon$. Such an error is very low and temperature compensation would not be necessary.
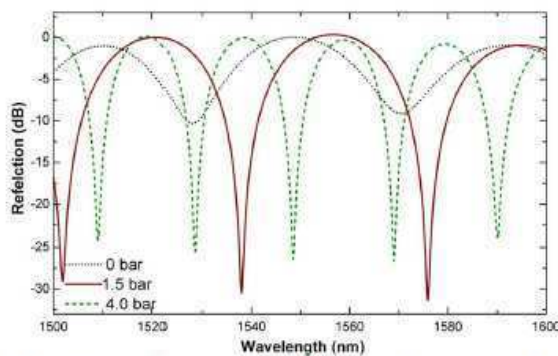

Fig. 3.   (Color online) Interference patterns observed when the PCF void is not pressurized (spherical cavity, $d = 27\,\mu$m) or pressurized (elliptical cavity) at 1.5 bars ($d = 28\,\mu$m) or at 4.0 bars ($d = 58\,\mu$m). In all cases the fiber was the PCF-B.
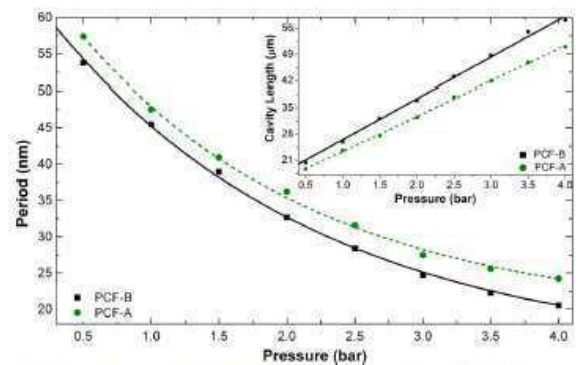

Fig. 4.   (Color online) Period of the FPIs as a function of the pressure in the voids of the PCF. The inset shows the cavity length as a function of pressure. The fibers used are indicated.
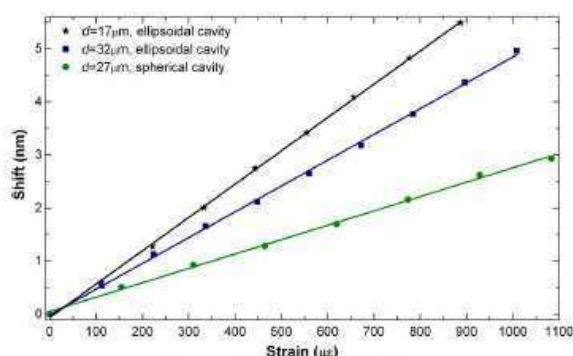
Fig. 5. (Color online) Shifts of the interference patterns as a function of strain in FPIs with ellipsoidal cavities of different sizes. For comparison, the response of a FPI with a spherical cavity is shown.

In conclusion, we have reported on the fabrication of microscopic FPIs in which the cavity is an air bubble trapped inside an optical fiber. Such a cavity is formed by fusion splicing together a standard SMF and a PCF. The voids of the PCF are pressurized in a controlled manner to achieve high reproducibility and control over the cavity length. It was found that the size of the PCF voids help to control the cavity dimensions. Our FPIs exhibited visibilities as high as 0.999 due to their ellipsoidal shape, which arises due to pressurization of the PCF and the splicing conditions. The sensing capabilities of the devices were investigated. High strain sensitivities and low temperature sensitivities were observed, thus suggesting that temperature compensation may not be required.

References

1. Y. J. Rao, Opt. Fiber Technol. **12**, 227 (2006).
2. J. Wang, B. Dong, E. Lally, J. Gong, M. Han, and A. Wang, Opt. Lett. **35**, 619 (2010).
3. X. Chen, F. Shen, Z. Wang, Z. Huang, and A. Wang, Appl. Opt. **45**, 7760 (2006).
4. V. R. Machavaram, R. A. Badcock, and G. F. Fernando, Sens. Actuators A **138**, 248 (2007).
5. E. Cibula and D. Donlagic, Opt. Express **15**, 8719 (2007).
6. Z. L. Ran, Y. J. Rao, H. Y. Deng, and X. Liao, Opt. Lett. **32**, 3071 (2007).
7. T. Wei, Y. Han, H.-L. Tsai, and H. Xiao, Opt. Lett. **33**, 536 (2008).
8. J. S. Sirkis, D. D. Brennan, M. A. Putman, T. A. Berkoff, A. D. Kersey, and E. J. Friebele, Opt. Lett. **18**, 1973 (1993).
9. Q. Shi, F. Lv, Z. Wang, L. Jin, J. J. Hu, Z. Liu, G. Kai, and X. Dong, IEEE Photon. Technol. Lett. **20**, 237 (2008).
10. O. Frazao, S. H. Aref, J. M. Baptista, J. L. Santos, H. Latifi, F. Farahi, J. Kobelke, and K. Schuster, IEEE Photon. Technol. Lett. **21**, 1229 (2009).
11. C. Wu, H. Y. Fu, K. K. Qureshi, B.-O. Guan, and H. Y. Tam, Opt. Lett. **36**, 412 (2011).
12. E. Li, G. D. Peng, and X. Ding, Appl. Phys. Lett. **92**, 101117 (2008).
13. J. Villatoro, V. Finazzi, G. Coviello, and V. Pruneri, Opt. Lett. **34**, 2441 (2009).
14. J. Ma, J. Ju, L. Jin, W. Jin, and D. Wang, Opt. Express **19**, 12418 (2011).
15. Y. Zhang, Y. Li, T. Wei, X. Lan, Y. Huang, G. Chen, and H. Xiao, IEEE Photon. J. **2**, 469 (2010).
16. A. S. Gerges, T. P. Newson, F. Farahi, J. D. C. Jones, and D. A. Jackson, Opt. Commun. **68**, 157 (1988).
17. W. Wadsworth, A. Witkowska, S. Leon-Saval, and T. Birks, Opt. Express **13**, 6541 (2005).

Spheroidal Fabry-Perot microcavities in optical fibers for high-sensitivity sensing

F. C. Favero,[1,2] L. Araujo,[1] G. Bouwmans,[3] V. Finazzi,[2] J. Villatoro,[2,*] and V. Pruneri[2,4]

[1]*Pontifical Catholic University of Rio de Janeiro, Rua Marquês de São Vicente 225, 22453-900, Rio de Janeiro, RJ, Brazil*
[2]*ICFO- Institut de Ciencies Fotoniques, Mediterranean Technolgy Park, 08860, Castelldefels, Barcelona, Spain*
[3]*PhLAM/IRCICA, Université Lille, CNRS UMR8523/USR3380, 59658 Villeneuve d'Ascq, France*
[4]*Also with ICREA-Institució Catalana de Recerca i Estudis Avançats, 08010, Barcelona, Spain*
[*] *joel.villatoro@icfo.es*

Abstract: All-optical-fiber Fabry-Perot interferometers (FPIs) with microcavities of different shapes were investigated. It was found that the size and shape of the cavity plays an important role on the performance of these interferometers. To corroborate the analysis, FPIs with spheroidal cavities were fabricated by splicing a photonic crystal fiber (PCF) with large voids and a conventional single mode fiber (SMF), using an ad hoc splicing program. It was found that the strain sensitivity of FPIs with spheroidal cavities can be controlled through the dimensions of the spheroid. For example, a FPI whose cavity had a size of ~10x60 μm exhibited strain sensitivity of ~10.3 pm/με and fringe contrast of ~38 dB. Such strain sensitivity is ~10 times larger than that of the popular fiber Bragg gratings (~1.2 pm/με) and higher than that of most low-finesse FPIs. The thermal sensitivity of our FPIs is extremely low (~1pm/°C) due to the air cavities. Thus, a number of temperature-independent ultra-sensitive microscopic sensors can be devised with the interferometers here proposed since many parameters can be converted to strain. To this end, simple vibration sensors are demonstrated.

References and links

1. Y.-J. Rao, "Recent progress in fiber-optic extrinsic Fabry–Perot interferometric sensors," Opt. Fiber Technol. **12**(3), 227–237 (2006).
2. J.-H. Chen, X.-G. Huang, and Z.-J. Huang, "Simple thin-film fiber optic temperature sensor based on Fabry-Perot interference," Opt. Eng. **49**(4), 044402 (2010).
3. C. Lee, L. Lee, H. Hwang, and J. Hsu, "Highly sensitive air-gap fiber Fabry-Perot interferometers based on polymer-filled hollow core fibers," IEEE Photon. Technol. Lett. **24**(2), 149–151 (2012).
4. N. V. Wheeler, M. D. W. Grogan, T. D. Bradley, F. Couny, T. A. Birks, and F. Benabid, "Multipass hollow core-pcf microcell using a tapered micromirror," J. Lightwave Technol. **29**(9), 1314–1318 (2011).
5. S. Pevec and D. Donlagic, "All-fiber, long-active-length Fabry-Perot strain sensor," Opt. Express **19**(16), 15641–15651 (2011).
6. C. Tuck, R. Hague, and C. Doyle, "Low cost optical fibre based Fabry–Perot strain sensor production," Meas. Sci. Technol. **17**(8), 2206–2212 (2006).
7. X. Chen, F. Shen, Z. Wang, Z. Huang, and A. Wang, "Micro-air-gap based intrinsic Fabry-Perot interferometric fiber-optic sensor," Appl. Opt. **45**(30), 7760–7766 (2006).
8. E. Cibula and D. Donlagic, "In-line short cavity Fabry-Perot strain sensor for quasi distributed measurement utilizing standard OTDR," Opt. Express **15**(14), 8719–8730 (2007).
9. Y.-J. Rao, M. Deng, D.-W, Duan, X.-C. Yang, T. Zhu, and G.-H. Cheng, "Micro Fabry-Perot interferometers in silica fibers machined by femtosecond laser," Opt. Express **15**(21), 14123–14128 (2007).
10. T. Wei, Y. Han, Y. Li, H.-L. Tsai, and H. Xiao, "Temperature-insensitive miniaturized fiber inline Fabry-Perot interferometer for highly sensitive refractive index measurement," Opt. Express **16**(8), 5764–5769 (2008).
11. J. Sirkis, T. A. Berkoff, R. T. Jones, H. Singh, A. D. Kersey, E. J. Friebele, and M. A. Putnam, "In-Line fiber etalon (ILFE) fiber-optic strain sensors," J. Lightwave Technol. **13**(7), 1256–1263 (1995).
12. Y. J. Rao, T. Zhu, X. C. Yang, and D. W. Duan, "In-line fiber-optic etalon formed by hollow-core photonic crystal fiber," Opt. Lett. **32**(18), 2662–2664 (2007).

13. Q. Shi, Z. Wang, L. Jin, Y. Li, H. Zhang, F. Lu, G. Kai, and X. Dong, "A hollow-core photonic crystal fiber cavity based multiplexed Fabry–Pérot interferometric strain sensor system," IEEE Photon. Technol. Lett. **20**(15), 1329–1331 (2008).
14. E. Li, G. D. Peng, and X. Ding, "High spatial resolution fiber-optic Fizeau interferometric strain sensor based on an in-fiber spherical microcavity," Appl. Phys. Lett. **92**(10), 101117 (2008).
15. J. Villatoro, V. Finazzi, G. Coviello, and V. Pruneri, "Photonic-crystal-fiber-enabled micro-Fabry-Perot interferometer," Opt. Lett. **34**(16), 2441–2443 (2009).
16. F. C. Favero, G. Bouwmans, V. Finazzi, J. Villatoro, and V. Pruneri, "Fabry-Perot interferometers built by photonic crystal fiber pressurization during fusion splicing," Opt. Lett. **36**(21), 4191–4193 (2011).
17. A. D. Kersey, M. A. Davis, H. J. Patrick, M. LeBlanc, K. P. Koo, C. G. Askins, M. A. Putnam, and E. J. Friebele, "Fiber grating sensors," J. Lightwave Technol. **15**(8), 1442–1463 (1997).
18. A. Laudati, F. Mennella, M. Giordano, G. D'Altrui, C. Calisti Tassini, and A. Cusano, "A fiber-optic Bragg grating seismic sensor," IEEE Photon. Technol. Lett. **19**(24), 1991–1993 (2007).
19. T. Guo, A. Ivanov, C. Chen, and J. Albert, "Temperature-independent tilted fiber grating vibration sensor based on cladding-core recoupling," Opt. Lett. **33**(9), 1004–1006 (2008).
20. M. Kamata, M. Obara, R. R. Gattass, L. R. Cerami, and E. Mazur, "Optical vibration sensor fabricated by femtosecond laser micromachining," Appl. Phys. Lett. **87**(5), 051106 (2005).
21. T. Ke, T. Zhu, Y. J. Rao, and M. Deng, "Accelerometer based on all-fiber Fabry-Perot interferometer formed by hollow-core photonic crystal fiber," Microw. Opt. Technol. Lett. **52**(11), 2531–2535 (2010).

1. Introduction

The Fabry-Perot interferometer (FPI) is one of the most versatile interferometers since it can be implemented in many different ways, see for example [1]. In its simplest configuration the quoted interferometer can be implemented with Fresnel reflections from two air-glass or glass-dielectric interfaces separated by a microscopic distance [2–5]. To avoid alignment elements and minimize the fabrication steps, monolithic fiber FPIs have been proposed in which a cavity is made by means of chemical etching [6–8], femto-second laser machining [9,10], or by inserting a short segment of hollow fiber or tube between optical fibers [11–13]. Another possibility to make alignment-free FPIs is by fusion splicing a photonic crystal fiber (PCF) and a standard optical fiber together [14–16]. All the aforementioned FPIs can be good choices for optical sensing since a minute change of the cavity size or index leads to a detectable shift of the interference pattern. The sensitivities achieved with most low-finesse FPIs reported until now are comparable to that of the popular fiber Bragg gratings (FBG). To the authors' best knowledge, no mechanism to enhance the sensitivity of FPIs while keeping their main advantages (microscopic size, robustness, minimal fabrication steps, etc.) has been proposed so far.

Here, we show that the shape and dimensions of the cavity help to substantially enhance the performance of a fiber FPI. Interferometers with cavities of spherical and spheroidal shapes are analyzed theoretically but the analysis of interferometers with cavities of other shapes is straightforward. We demonstrate a FPI with spheroidal cavity of size ~10x60 μm that exhibited fringe contrast of 38 dB (visibility of 0.99984). We believe that such visibility is the highest one ever reported for a low-finesse FPI. In addition to the high visibility, the referred device exhibited a strain sensitivity of ~10.3 pm/με which is ~10 times higher than that of the popular FBG (~1.2pm/με) [17] and higher than that of most low-finesse FPIs previously reported. To achieve FPIs with spheroidal cavities we fusion spliced a properly-selected PCF to a single mode optical fiber (SMF) with an on-purpose splicing program.

2. Theoretical analysis

Let us assume a FPI whose cavity is made of air, has quasi-spherical ($r \approx d$) or spheroidal shape and that is completed embedded in an optical fiber whose diameter is $2R$, see Fig. 1. In
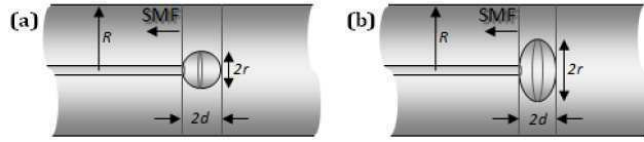
Fig. 1. Diagram of a Fabry-Perot interferometer with (a) spherical and (b) spheroidal air cavities which are assumed to be at the end of a single mode fiber (SMF), in front of its core.

the following analysis an oblate spheroid, *i.e.*, an ellipse rotated around its minor axis, with size of $2d \times 2r$ ($r > d$) will be assumed, where $2d$ is the polar diameter and r the equator radius. Note that the spheroid polar axis (equator plane) is assumed to coincide with the direction of light propagation. Light reflected from the SMF-air interface and that reflected from the air-glass interface can be coupled back into the SMF and interfere. The accumulated phase difference between the two Fresnel reflections is $\varphi \approx 4\pi n d/\lambda + \pi$, where λ is the wavelength of the optical source and n the refractive index of the medium inside the cavity. Thus, if one launches light from a broadband source to the cavity and the reflection is analyzed with a spectrometer a series of maxima and minima (interference pattern) can be expected. The maxima will appear whenever $\varphi = 2\pi m$, with m a strictly positive integer. This means, at wavelengths that satisfy the condition: $\lambda_m = 2nd/(m-1/2)$.

Like a FPI with flat reflecting surfaces, a FPI with spherical or spheroidal cavity can be used for sensing physical parameters such as strain ($\delta d/d$) and any other parameter that can be transduced to strain, *e.g.*, pressure, load, vibration, tilt, etc. Any of these parameters will induce solely a minute change of the cavity size since the cavity is assumed to be made of air ($n = 1$). The changes experienced by the interferometer cavity will result in a shift in the position of the interference maxima (or minima) by $\delta\lambda_m$. To correlate the shift of the interference pattern with the change of the cavity size hence to estimate the sensitivity, it is necessary to differentiate λ_m. This leads to the simple expression: $\delta\lambda_m = \lambda_m(\delta d/d)$. Most authors assume that the strain sensitivity of a FPI is independent of the cavity size and that it can be enhanced solely by choosing longer wavelengths. Recent results reported by our group in [15] and [16] suggest that the cavity size and shape of a FPI plays an important role in the interferometer performance and motivated the work here presented.

If a FPI with cavities like those described in Fig. 1 is subjected to axial strain, force or pressure it will experience the so-called Poisson effect which states that if d changes by δd then r will change by δr. Thus, an axial strain ($\varepsilon_a = \delta d/d$) applied to the cavity will induce a transversal strain ($\varepsilon_t = \delta r/r$) to the same. The axial and the transversal strains are related to each other by means of the Poisson's ratio ($\nu = -\varepsilon_t/\varepsilon_a$). Thus, the shift of the interference pattern of a FPI with quasi-spherical or spheroidal cavity depends on ν which in turn is proportional to $dr/\delta d$. To calculate the Poisson's ratio we need to analyze the volume (V) of the section of optical fiber that contains the cavity and its microscopic changes (δV). If δV is caused for example by changes of pressure and temperature, then the following expression is fulfilled:

$$\frac{\delta V}{V} = \frac{-1}{K}\delta P + \gamma \delta T. \qquad (1)$$

In Eq. (1), K is the bulk modulus and γ is the coefficient of thermal expansion. Let us assume that the change in pressure is due to axial strain applied to the optical fiber. Thus, pressure and strain are related by means of the Young's modulus $E = \sigma/\varepsilon_a = \delta P/\varepsilon_a$, (where σ is the tensile stress and ε_a is the axial strain). The volumetric changes caused by temperature can be

Microstructured optical fiber interferometric breathing sensor

Fernando C. Favero,[a,b] **Joel Villatoro,**[b] **and Valerio Pruneri**[b,c]
[a]Pontifical Catholic University of Rio de Janeiro, Rua Marquês de São Vicente 225, 22453–900, Rio de Janeiro, Brazil
[b]ICFO-The Institute of Photonic Sciences, Mediterranean Technology Park, Av. Carl Friedrich Gauss, number 3, 08860 Castelldefels, Barcelona, Spain
[c]ICREA-Institució Catalana de Recerca i Estudis Avançats, 08010, Barcelona, Spain

Abstract. In this paper a simple photonic crystal fiber (PCF) interferometric breathing sensor is introduced. The interferometer consists of a section of PCF fusion spliced at the distal end of a standard telecommunications optical fiber. Two collapsed regions in the PCF caused by the splicing process allow the excitation and recombination of a core and a cladding PCF mode. As a result, the reflection spectrum of the device exhibits a sinusoidal interference pattern that instantly shifts when water molecules, present in exhaled air, are adsorbed on or desorbed from the PCF surface. The device can be used to monitor a person's breathing whatever the respiration rate. The device here proposed could be particularly important in applications where electronic sensors fail or are not recommended. It may also be useful in the evaluation of a person's health and even in the diagnosis and study of the progression of serious illnesses such as sleep apnea syndrome. © *2012 Society of Photo-Optical Instrumentation Engineers (SPIE).* [DOI: 10.1117/1.JBO.17.3.037006]

Keywords: fiber optic sensors; interferometers; interferometry; optical breathing sensors.

Paper 11503 received Sep. 13, 2011; revised manuscript received Jan. 5, 2012; accepted for publication Jan. 13, 2012; published online Mar. 23, 2012.

1 Introduction

Breathing is a human vital sign, thus its monitoring is important during certain imaging and surgical procedures where the patient needs to be sedated or anesthetized.[1] On the other hand, some serious illnesses (e. g. sleep apnea syndrome) can be diagnosed by detecting alterations in breathing rates or abnormal respiratory rate.[2] Monitoring of breathing is also important to study the progression of a diagnosed illness or to evaluate the health of a person.

Breathing can be detected and analyzed using different methods. The most popular ones involve electronic sensors, see for example Refs. 3 and 4. Electronic breathing sensors are not recommended when patients are, for example, in a magnetic resonance imaging (MRI) system, or during any oncological treatment that requires the administration of radiation or high electric/magnetic fields since they can fail and also represent a burning hazard to the patient. In the aforementioned conditions optical breathing sensors are good candidates. Breathing can be monitored, for example, using fiber-based humidity or temperature sensors placed close to the patient's nose or mouth since the air exhaled by these airways has higher humidity and is warmer than the inhaled air.[5-9] Another alternative to monitor breathing using optical fiber sensors is by detecting the contraction and expansion of the patient's chest and abdomen that occur during breathing.[10-14] This can be done by means of highly-sensitive strain, bending or pressure sensors set in a belt, strap or patch attached to the patient's body.[10-14]

The advantages of fiberoptic sensors for monitoring breathing and other parameters of clinical relevance include their small size, bio- and electromagnetic compatibility and greater

flexibility. Some drawbacks of the existing fiber-based breathing sensors include the need of temperature/humidity-sensitive thin films which usually degrade over time or respond too slowly to changes in humidity/temperature. On the other hand, some fiber-based strain/bending sensors are also sensitive to body motions, thus, in some circumstances; it can be difficult to distinguish breathing from a person's involuntary motions.

In this work we report on a simple optical fiber interferometric breathing sensor that does not required any kind of breathing-sensitive thin film or layer. The device operates in reflection mode and consists of a short segment of photonic crystal fiber (PCF), also known as microstructured or holey optical fiber, fusion spliced at the distal end of a standard optical fiber. A core and a cladding mode are excited and recombined in the PCF. As a result, the reflection spectrum of the device exhibits a well-defined interference pattern. The cladding mode is highly sensitive to water molecules adsorbed on the PCF surface. Thus, when a person exhales air close to the interferometer an instant shift of the interference pattern is observed. The device here proposed may be used to monitor a person's breathing whatever the respiration rate.

2 Device Fabrication and Performance

Figure 1 shows schematic drawings of the proposed device along with some details of the interrogation set up. The fabrication of the interferometer is simple and straightforward since it only involves cleaving and fusion splicing, which can be carried out with common fiber tools and equipment.[15] A micrograph of the PCF cross section is shown in the figure. The fiber is commercially available and it is known as large-mode-area PCF (LMA-10, NKT Photonics). This fiber has six-fold symmetry; its core and outer diameters are, respectively, 10 and

Address all correspondence to: Joel Villatoro, ICFO—The Institute of Photonic Sciences, Mediterranean Technology Park, Av. Carl Friedrich Gauss, num. 3, 08860 Castelldefels, Barcelona, Spain, Tel: 34935534137; Fax: 34 935534000; E-mail: joel.villatoro@icfo.es

Favero, Villatoro, and Pruneri: Microstructured optical fiber interferometric breathing sensor
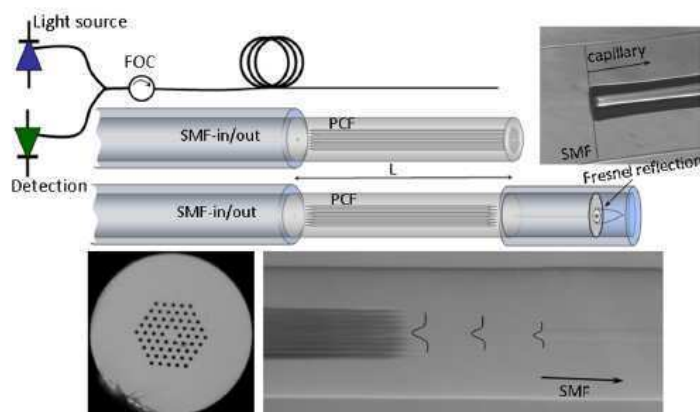

Fig. 1 Schematic diagram for interrogating the interferometer. The drawings show the interferometer with an "open void" or a "sealed void" configuration. *L* is the length of PCF. The micrographs show the PCF cross section and the PCF-SMF or SMF-capillary junctions. The broadening of the fundamental SMF mode is also illustrated.

125 μm. The diameter of the voids is 3.1 μm and the separation between consecutive voids (pitch) is 6.6 μm. A short section (between 1 to 2 cm) of PCF was fusion spliced at the end of a standard telecommunication optical fiber (SMF-28). A conventional splicing machine (Ericsson FSU 955) was used to fabricate the devices. The default programs set in such a machine for splicing single mode fibers can be used to splice the SMF and the PCF. Under these conditions a robust and permanent join is achieved. However, the PCF's voids fully collapse over a length of a few hundred micrometers because the softening point of PCFs is lower than that of SMFs due to their holey structure. The length of the collapsed zone in the PCF can be shortened without compromising the robustness of the splice by properly reducing the intensity and duration of the arc discharge.[16] Figure 1 shows a micrograph of the SMF-PCF junction with a 130 μm-long collapsed zone.

The collapsed region in the PCF is what allows the excitation and recombination of modes, thus achieving an interferometer. The propagating beam goes through a section without core or voids when it travels through the SMF-PCF junction. When the fundamental SMF-in mode enters the collapsed region of the PCF, it immediately broadens due to diffraction, as seen in Fig. 1. The broadening introduces a mode field mismatch which combined with the modal properties of the PCF allows the excitation of specific modes in the PCF.[16] Owing to the axial symmetry the excited modes are those that have similar azimuthal symmetry, i.e., the HE_{11} core mode and the HE_{22}-like cladding mode.[16] Such modes have different effective refractive indices and propagate at different phase velocities; hence they accumulate a phase difference. If the effective index of the HE_{11} core mode is n_1 and n_2 is that of the HE_{22} cladding mode, then the phase difference will be $\Delta\phi \cong 2\pi\Delta n/L$, with $\Delta n = n_1 - n_2$ and L the length of PCF. The effective indices, and therefore, the phase difference $\Delta\phi$ depend on the wavelength (λ) of the optical source. If the modes are reflected from the PCF cleaved end, as seen in the "open void" configuration in Fig. 1, the accumulated phase difference will be $\Delta\phi \cong 4\pi\Delta n/L$ due to the double pass over the PCF.[17,18] When the reflected modes reach the collapsed region they will

be recombined into a SMF core mode. Thus, if one launches light from a broadband optical source, e.g. an light emitting diode (LED), to the device and the output light is fed to a spectrometer, the resulting spectrum will exhibit a series of maxima and minima, i.e. an interference pattern as it is shown in Fig. 2(a).
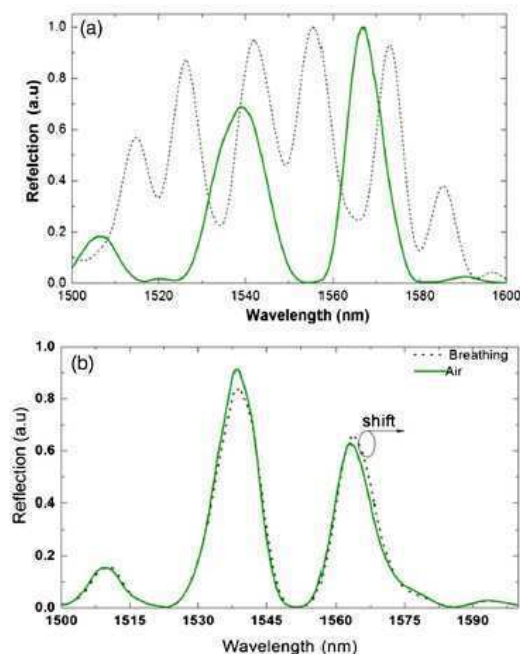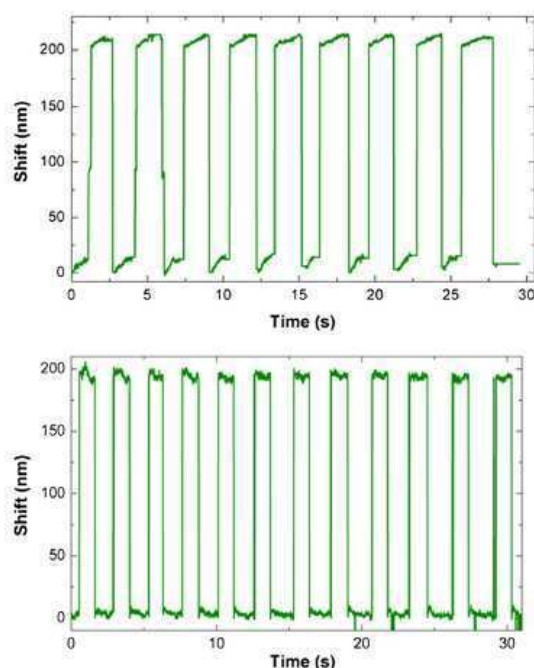

Fig. 2 (a) Normalized reflection spectra of an interferometer with in an open void configuration (dotted line) and in a sealed void one (solid line). (b) Reflection spectrum of a sealed-void interferometer when the external medium was air (solid line) and when a person breathed close to it (dotted line). In all cases the length of PCF was 20 mm.
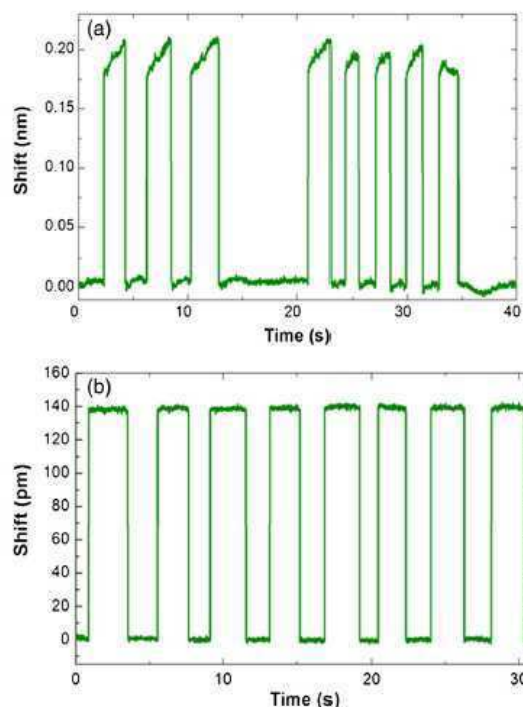
was placed over his nose and mouth and his breathing was again monitored. Figure 4 shows the observed shift versus time. It can be noted that the device responds well whatever the respiration cycle. In another test, the volunteer was asked to breathe normally and then to stop breathing during a few seconds. Figure 5(a) shows the results under these breathing conditions. It can be noted that the shift is nearly zero during the entire time the volunteer did not breathe. The results shown in Fig. 5(a) suggest that our device might be useful in the study or diagnosis of sleep apnea syndrome, an illness characterized by abnormal pauses in breathing or instances of abnormally low breathing during sleep.

To investigate the reusability of our sensor, the breathing of another volunteer was monitored; the results are shown in Fig. 5(b). The monitoring was carried out with the same procedure described above. Note that the shift is not exactly the same in all cases due to variation in the separation between the person's nose and the sensor, and also to possible contamination of the sensitive part of the interferometer. However, information about the person's respiration rate, an important indicator of a person's health, is obtained. The contamination issue can be overcome by cleaning the sensor with commercially available solvents or even with sterilization of the device since optical fibers can be sterilized but fluctuations of the separation between nose and sensor cannot be eliminated.

The results discussed above are promising, because they indicate that our device can follow the breathing cycles whatever the respiration rate or condition. However, for the device to be useful as a patient respiratory sensor in a real medical setting it would need to fulfill more requirements. For example, the limitations in size were analyzed by fabricating interferometers of
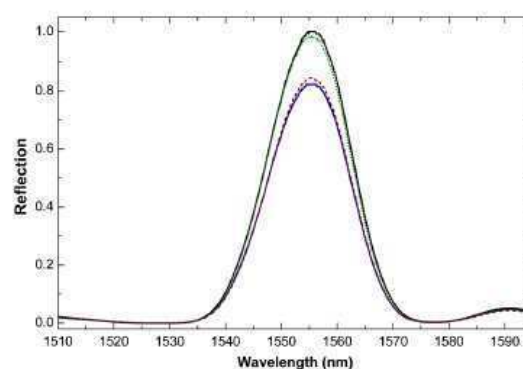

Fig. 5 (a) Shift of the interference pattern when a person, on purposefully, stopped breathing during a few seconds. (b) Shift of the interference pattern observed when another volunteer was breathing normally. In both cases a 20-mm-long sealed-void interferometer was used and the wavelength was 1550 nm.

different lengths. Possible failure modes were also investigated. Figure 6 shows the interference pattern observed in a 12-mm-long device when the fiber cable was subjected to movements and bending which typically can be caused by motion of the patient. Although the intensity of the pattern fluctuates the position of the peak remains unaltered. This suggests that voluntary
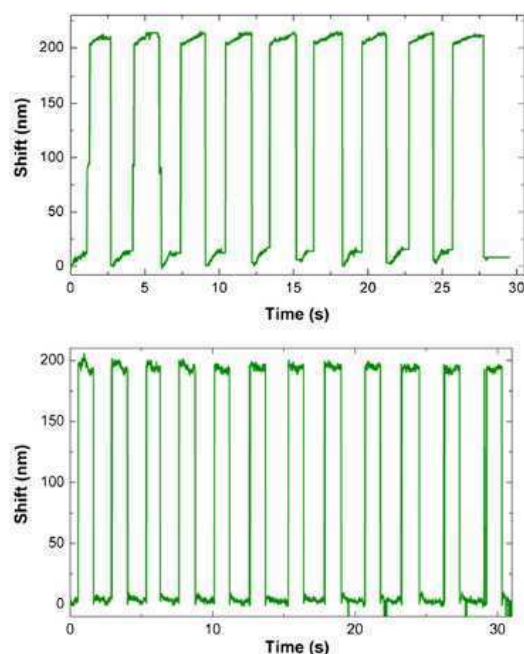

Fig. 4 Shift of the interference pattern observed when the volunteer's heart beat rate was 110 bpm (top graph) and 135 bpm (bottom graph). In both cases a 20-mm-long sealed-void interferometer was used and the wavelength was 1550 ± 50 nm.

Fig. 6 Interference patterns observed when the fiber was subjected to bending and movements. Each trace is the result from a different position. The length of PCF was 12 mm. The intensity changes but the position of the peak remains unaltered.
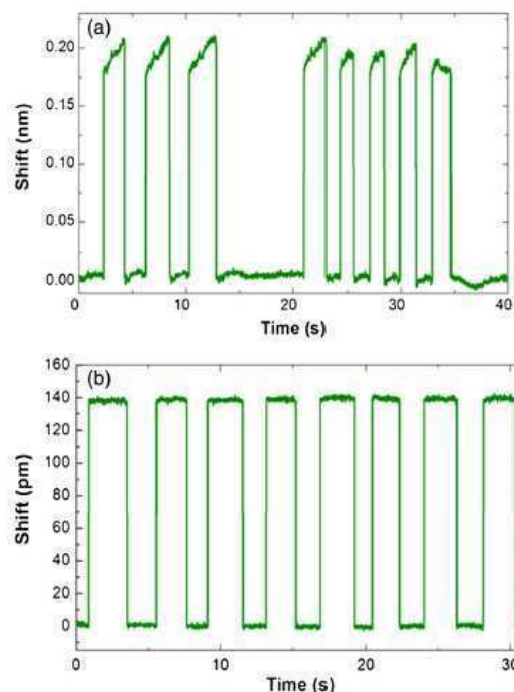
was placed over his nose and mouth and his breathing was again monitored. Figure 4 shows the observed shift versus time. It can be noted that the device responds well whatever the respiration cycle. In another test, the volunteer was asked to breathe normally and then to stop breathing during a few seconds. Figure 5(a) shows the results under these breathing conditions. It can be noted that the shift is nearly zero during the entire time the volunteer did not breathe. The results shown in Fig. 5(a) suggest that our device might be useful in the study or diagnosis of sleep apnea syndrome, an illness characterized by abnormal pauses in breathing or instances of abnormally low breathing during sleep.

To investigate the reusability of our sensor, the breathing of another volunteer was monitored; the results are shown in Fig. 5(b). The monitoring was carried out with the same procedure described above. Note that the shift is not exactly the same in all cases due to variation in the separation between the person's nose and the sensor, and also to possible contamination of the sensitive part of the interferometer. However, information about the person's respiration rate, an important indicator of a person's health, is obtained. The contamination issue can be overcome by cleaning the sensor with commercially available solvents or even with sterilization of the device since optical fibers can be sterilized but fluctuations of the separation between nose and sensor cannot be eliminated.

The results discussed above are promising, because they indicate that our device can follow the breathing cycles whatever the respiration rate or condition. However, for the device to be useful as a patient respiratory sensor in a real medical setting it would need to fulfill more requirements. For example, the limitations in size were analyzed by fabricating interferometers of
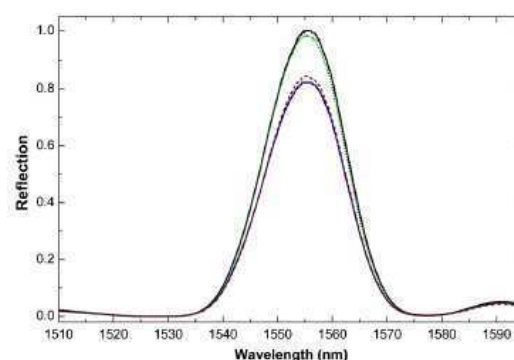

Fig. 4 Shift of the interference pattern observed when the volunteer's heart beat rate was 110 bpm (top graph) and 135 bpm (bottom graph). In both cases a 20-mm-long sealed-void interferometer was used and the wavelength was 1550 ± 50 nm.

Fig. 5 (a) Shift of the interference pattern when a person, on purposefully, stopped breathing during a few seconds. (b) Shift of the interference pattern observed when another volunteer was breathing normally. In both cases a 20-mm-long sealed-void interferometer was used and the wavelength was 1550 nm.

different lengths. Possible failure modes were also investigated. Figure 6 shows the interference pattern observed in a 12-mm-long device when the fiber cable was subjected to movements and bending which typically can be caused by motion of the patient. Although the intensity of the pattern fluctuates the position of the peak remains unaltered. This suggests that voluntary

Fig. 6 Interference patterns observed when the fiber was subjected to bending and movements. Each trace is the result from a different position. The length of PCF was 12 mm. The intensity changes but the position of the peak remains unaltered.

or involuntary motions of the patient or fiber cable may not affect the measurements. Another possible failure mode is when a person coughs or contaminates the device with fluids (saliva, sputum, etc.). However, these issues can be avoided or overcome by embedding the device in a nasal clip, adequate packaging, or using a cleaning process.

4 Conclusions

In this work we report on a breathing sensor based on a photonic crystal fiber interferometer that operates in reflection mode. The fabrication of the device is simple since it involves a pair of fusion splices, hence it can be carried out with conventional fiber tools and instruments. The cost of the devices is low because the components (optical fibers) are inexpensive and widely available. The key part of the interferometer is a microscopic collapsed region in the PCF which is what allows the excitation and recombination of two modes in the PCF. One of the modes (the cladding mode) is highly sensitive to changes of refractive index on the PCF surface. Thus, when water vapor from exhaled air is present on the PCF surface, the interference pattern shifts. Such a shift can be detected in real time. Our results suggest that the device can be used to monitor a person's breathing whatever the breathing rate is. All the components of the interferometer are (or can be made of) dielectric materials, thus, the device can be used in critical applications, such as during magnetic resonance imaging or some oncological treatments, where electrical breathing sensors may not operate properly or are not recommended because of potential burning hazards. The device here proposed can also be useful in the diagnosis of serious illnesses such as sleep apnea syndrome.

Development of a portable breathing monitor is feasible because of considerable advances in the development of miniature light sources and detectors. Compact and portable FBG interrogator units are emerging. Thus, in the near future the breathing sensors here proposed might be incorporated into battery-operated portable medical diagnostic equipment.

References

1. M. Folke et al., "Critical review of non-invasive respiratory monitoring in medical care," *Med. Biol. Eng. Comput.* **41**(4), 377–383 (2003).
2. P. Várady et al., "A novel method for the detection of apnea and hypopnea events in respiration signals," *IEEE Trans. Biomed. Eng.* **49**(9), 936–942 (2002).
3. P. Corbishley and E. Rodríguez-Villegas, "Breathing detection: towards a miniaturized, wearable, battery-operated monitoring system," *IEEE Trans. Biomed. Eng.* **55**(1), 196–204 (2008).
4. F. Q. AL-Khalidi et al., "Respiration rate monitoring methods: a review," *Pediatr. Pulm.* **46**(6), 523–529 (2011).
5. S. Muto, H. Sato, and T. Hosaka, "Optical humidity sensor using fluorescent plastic fiber and its application to breathing-condition monitor," *Jpn. J. Appl. Phys.* **33**(10), 6060–6064 (1994).
6. F. J. Arreguil et al., "Optical fiber humidity sensor using a nano Fabry–Perot cavity formed by the ionic self-assembly method," *Sensor Actuat B -Chem.* **59**(1), 54–59 (1999).
7. Y. Kang et al., "Nanostructured optical fibre sensors for breathing airflow monitoring," *Meas. Sci. Technol.* **17**(5), 1207–1212 (2006).
8. W. J. Yoo et al., "Development of optical fiber-based respiration sensor for noninvasive respiratory monitoring," *Opt. Rev.* **18**(1), 132–138 (2011).
9. S. Akita, A. Seki, and K. Watanabe, "A monitoring of breathing using a hetero-core optical fiber sensor," *Proc. SPIE* **7981**, 79812W (2011).
10. A. Babchenko et al., "Fiber optic sensor for the measurement of respiratory chest circumference changes," *J. Biomed. Opt.* **4**(2), 224–229 (1999).
11. G. Wehrle et al., "A fiber optic Bragg grating strain sensor for monitoring ventilatory movements," *Meas. Sci. Technol.* **12**(7), 805–809 (2001).
12. A. Grillet et al., "Optical fiber sensors embedded into medical textiles for healthcare monitoring," *IEEE Sens. J.* **8**(7), 1215–1222 (2008).
13. M. Nishyama, M. Miyamoto, and K. Watanabe, "Respiration and body movement analysis during sleep in bed using hetero-core fiber optic pressure sensors without constraint to human activity," *J. Biomed. Opt.* **16**(1), 017002 (2011).
14. A. F. Silva et al., "Simultaneous cardiac and respiratory frequency measurement based on a single fiber Bragg grating sensor," *Meas. Sci. Technol.* **22**(7), 075801 (2011).
15. J. Villatoro et al., "Simple all-microstructured-optical-fiber interferometer built via fusion splicing," *Opt. Express* **15**(4), 1491–1496 (2007).
16. G. A. Cárdenas-Sevilla et al., "Photonic crystal fiber sensor array based on modes overlapping," *Opt. Express* **19**(8), 7596–7602 (2011).
17. J. Villatoro et al., "Photonic crystal fiber interferometer for chemical vapor detection with high sensitivity," *Opt. Express* **17**(3), 1447–1453 (2009).
18. J. Mathew et al., "Humidity sensor based on photonic crystal fibre interferometer," *Electron. Lett.* **46**(19), 1341–1343 (2010).
19. K. Tiefenthalera and W. Lukosz, "Grating couplers as integrated optical humidity and gas sensors," *Thin Solid Films* **126**(3–4), 205–211 (1985).
20. D. Monzón-Hernández et al., "Photonic crystal fiber microtaper supporting two selective higher-order modes with high sensitivity to gas molecules," *Appl. Phys. Lett.* **93**(8), 081106 (2008).